Langmuir

Article

pubs.acs.org/Langmuir

In Situ Experiments To Reveal the Role of Surface Feature Sidewalls in the Cassie–Wenzel Transition

René Hensel,*[,†] Andreas Finn,[‡] Ralf Helbig,[†] Sebastian Killge,[‡] Hans-Georg Braun,[†] and Carsten Werner*[,†,§]

[†]Max Bergmann Center of Biomaterials, Leibniz Institute of Polymer Research Dresden, 01069 Dresden, Germany

[‡]Institute of Semiconductors and Microsystems, Technische Universität Dresden, 01187 Dresden, Germany

[§]B CUBE Innovation Center for Molecular Bioengineering, Technische Universität Dresden, 01307 Dresden, Germany

Supporting Information

ABSTRACT: Waterproof and self-cleaning surfaces continue to attract much attention as they can be instrumental in various different technologies. Such surfaces are typically rough, allowing liquids to contact only the outermost tops of their asperities, with air being entrapped underneath. The formed solid–liquid–air interface is metastable and, hence, can be forced into a completely wetted solid surface. A detailed understanding of the wetting barrier and the dynamics of this transition is critically important for the practical use of the related surfaces. Toward this aim, wetting transitions were studied *in situ* at a set of patterned perfluoropolyether dimethacrylate (PFPEdma) polymer surfaces exhibiting surface features with different types of sidewall profiles. PFPEdma is intrinsically hydrophobic and exhibits a refractive index very similar to water. Upon immersion of the patterned surfaces into water, incident light was differently scattered at the solid–liquid–air and solid–liquid interface, which allows for distinguishing between both wetting states by dark-field microscopy. The wetting transition observed with this methodology was found to be determined by the sidewall profiles of the patterned structures. Partial recovery of the wetting was demonstrated to be induced by abrupt and continuous pressure reductions. A theoretical model based on Laplace's law was developed and applied, allowing for the analytical calculation of the transition barrier and the potential to revert the wetting upon pressure reduction.

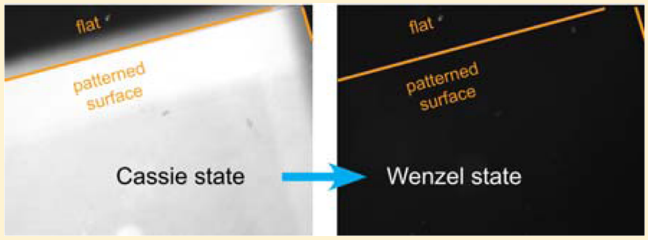

INTRODUCTION

Surface roughness has been shown to affect macroscopic surface wetting properties significantly since two different wetting regimes can coexist: In the Wenzel state, liquids entirely wet the surface, including the asperities and grooves of a rough surface, resulting in a homogeneous liquid–solid interface.[1] In contrast, in the Cassie state, liquids can be sustained at the asperities, and air is trapped inside the grooves (designated as plastron), resulting in a heterogeneous interface.[2] To predict the wetting state of any given system, minima in the Gibbs energy function of the three-phase solid–liquid–air system are analyzed.[3,4] While the Cassie state can be energetically more favorable than the Wenzel state it is only metastable. To induce the wetting transition from the Cassie to the Wenzel state, it requires to overcome an energetic barrier,[5−9] which can be possibly be achieved by the kinetic energy of impacting (rain) droplets,[10] an enhanced inner pressure of a droplet due to evaporation accompanied by shrinkage of the droplet size,[11] or even due to gravitational effects. Furthermore, the transition can be triggered by external stimuli such as compression of the liquid,[12−14] vibration,[15] or an external electrical field.[16] In view of numerous applications and products relying on waterproof and self-cleaning surfaces, which are essentially depend on the persistence of the Cassie state, a detailed understanding of the robustness of the Cassie state, the dynamics of the wetting transition, and the potential of a surface to recover the Cassie state upon partial wetting are of crucial interest.

Two different scenarios have been discussed for the Cassie–Wenzel transition, namely, sagging and depinning. Upon application of elevated pressure, the water–air interface sags into the grooves underneath, while the position of the three-phase contact line remains unchanged. The wetting transition occurs as soon as the sagging fluid front reaches the bottom of the groove. In depinning, the initial sagging enforces the depinning of the three-phase contact line from the edge of the asperity, which subsequently propagates along the sidewall until the liquid front reaches the bottom of the groove. The transition scenario, for example, can be controlled by the height of the surface features.[17] Furthermore, the transition dynamics as well as the transition barrier depend on topographical parameters of a rough surface: First, the distances between the surface features were shown to influence the wetting barrier.[18] Second, overhangs on the sidewalls of pillars or cavities can

Received: September 9, 2014
Revised: November 29, 2014
Published: December 12, 2014

   dx.doi.org/10.1021/la503601u | *Langmuir* 2014, 30, 15162−15170

restrict liquid expansion and were reported to enable the Cassie state even on intrinsically wettable surfaces.[19] Third, the implementation of "serifs" in overhangs of surface features was found to further enhance the wetting transition barrier due to the Laplace breakthrough scenario, which is independent of the surface chemistry of the solid surface.[20]

In previous studies, we developed a theoretical model allowing for the analytical calculation of the transition barrier, namely, Δp_{break}, the hydrostatic pressure needed for liquid breakthrough.[20] The model is based on the correlation of Laplace's law, Young's equation, and the Gibb's extension for a certain surface topography. Laplace's law describes the dependence of the pressure difference, Δp, across a curved fluid interface on γ, the interfacial energy of the water−air interface, and κ, the mean curvature of the interface:

$$\Delta p = 2\gamma\kappa \tag{1}$$

Young's equation represents the force balance acting at the three-phase contact line due to minimization of the Gibbs energy:

$$\cos\theta_Y = \frac{\gamma_{sg} - \gamma_{sl}}{\gamma} \tag{2}$$

where γ_{sg} and γ_{sl} are the solid−gas and the solid−liquid interfacial energies, respectively, and θ_Y is the intrinsic contact angle. The Gibb's extension further describes the pinning of an advancing or receding contact line at edges or wedges. This leads to a continuous variation of θ_a, the apparent contact angle at one given position (designated as canthotaxis effect):[21−23]

$$\theta_Y \le \theta_a \le \theta_Y + (\pi + \Psi) \tag{3}$$

where Ψ represents the geometrical edge angle (Figure 1), i.e., the slope along the cavity sidewall, which is the arctangent of the first derivative of a known sidewall function ($\Psi := \tan^{-1} f'(x)$). Note that throughout this work Ψ is displayed on the right-hand side of the cavities. The pressure to enforce the movement of the three-phase contact line results from the pressure difference, Δp, between p_h, the hydrostatic pressure of the applied liquid, and p_0, the atmospheric pressure of the entrapped air. Note that in the experiments demonstrated below the hydrostatic pressure is slowly increased with the speed of 10 hPa/s, and hence, the displaced air inside the cavities is dissolved in the liquid due to higher solubility at higher pressures or even diffuses into the substrate material due to the high gas permeability of the perfluoropolyether dimethacrylate (PFPEdma).[24] Both processes occur on a time scale much shorter than the elevation of the hydrostatic pressure. Consequently, for evolving the theoretical model, it is assumed that the expanding liquid front does not result in a compressed air reservoir inside the cavity (p_0 = constant). Applying eqs 1−3, Δp can be calculated as follows:

$$\Delta p = p_h - p_0 = \frac{2\gamma \sin(\theta_a - \pi)}{x} \tag{4}$$

Herein, it is supposed that the sagging interface has the shape of a spherical cap with a curvature, κ, which is given by $\kappa = (\sin(\theta_a - \pi))/x = 1/R$, where x denotes the distance between the three-phase contact point and the symmetry center ($x = 0$) of the cavity and R is the curvature radius of the fluid interface (cf. Figure 7a). Taking into account the maximal apparent contact angle $\theta_{a,max} = \theta_Y + (\pi + \Psi)$ occurring before the three-phase contact line depins,[20] the critical pressure difference can be expressed by

$$\Delta p_{break} = \frac{2\gamma \sin(\theta_Y + \Psi)}{x} \tag{5}$$

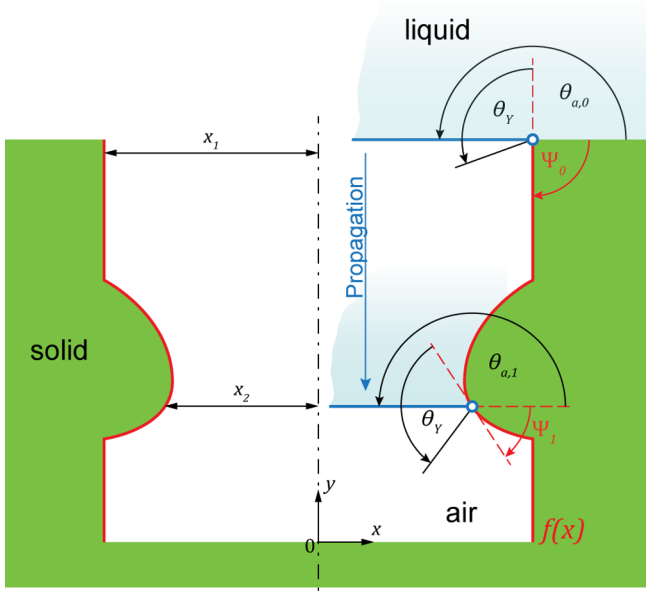

Figure 1. Cross-sectional view of a hydrophobic cavity with sidewall profile $f(x)$. First, the applied liquid is sustained atop the cavity with the half-width, x_1, the intrinsic contact angle, θ_Y, and the geometrical edge angle, Ψ_0, due to the fact that the apparent contact angle, θ_a, is smaller than $\theta_Y + (\pi + \Psi_0)$ (cf. eq 3). Second, upon partial propagation of the liquid front into the cavity, the half-width of the cavity and the geometrical edge angle change due to the scallop that constricts the cavity. Consequently, the barrier against the wetting transition changes in accordance with eq 5.

Various experimental approaches have been developed to observe the Cassie−Wenzel wetting transition. First, the (spontaneous) decrease of the macroscopic contact angle of an evaporating droplet deposited on a pillar was recorded.[18] However, this method provides insight neither into the dynamics of the impalement (vertical expansion of the liquid front) nor into the spreading of the meniscus across the surface (lateral expansion of the liquid front) that strongly depends on the pillar geometries and density.[25] Second, direct observations of droplet impalements onto pillar structures by interference microscopy, laser scanning confocal microscopy, synchrotron X-ray radiography, and high-frequency acoustic methods were used.[11,26−30] These methods directly allow for observing the interface deformation between adjacent pillars. It was found that the time scale of the transition can vary from slow sliding (within seconds to minutes) along the sidewall (i.e., the impalement) to abrupt propagation immediately after contact of the drop with the surface. However, the spatial and temporal resolution limits of these methods may restrict the applicability for nanoscopic surface features. An alternative consist of the indirect observation by integration of numerous identical surface features within a region of interest. Herein, spatial changes of the liquid−air interface are recorded by collecting the reflected or diffracted intensities of light.[13,31−33]

As all previously reported studies focus on the transition dynamics for pillar surfaces with straight sidewalls a comprehensive analysis of complex-shaped sidewalls as well

dx.doi.org/10.1021/la503601u | Langmuir 2014, 30, 15162−15170

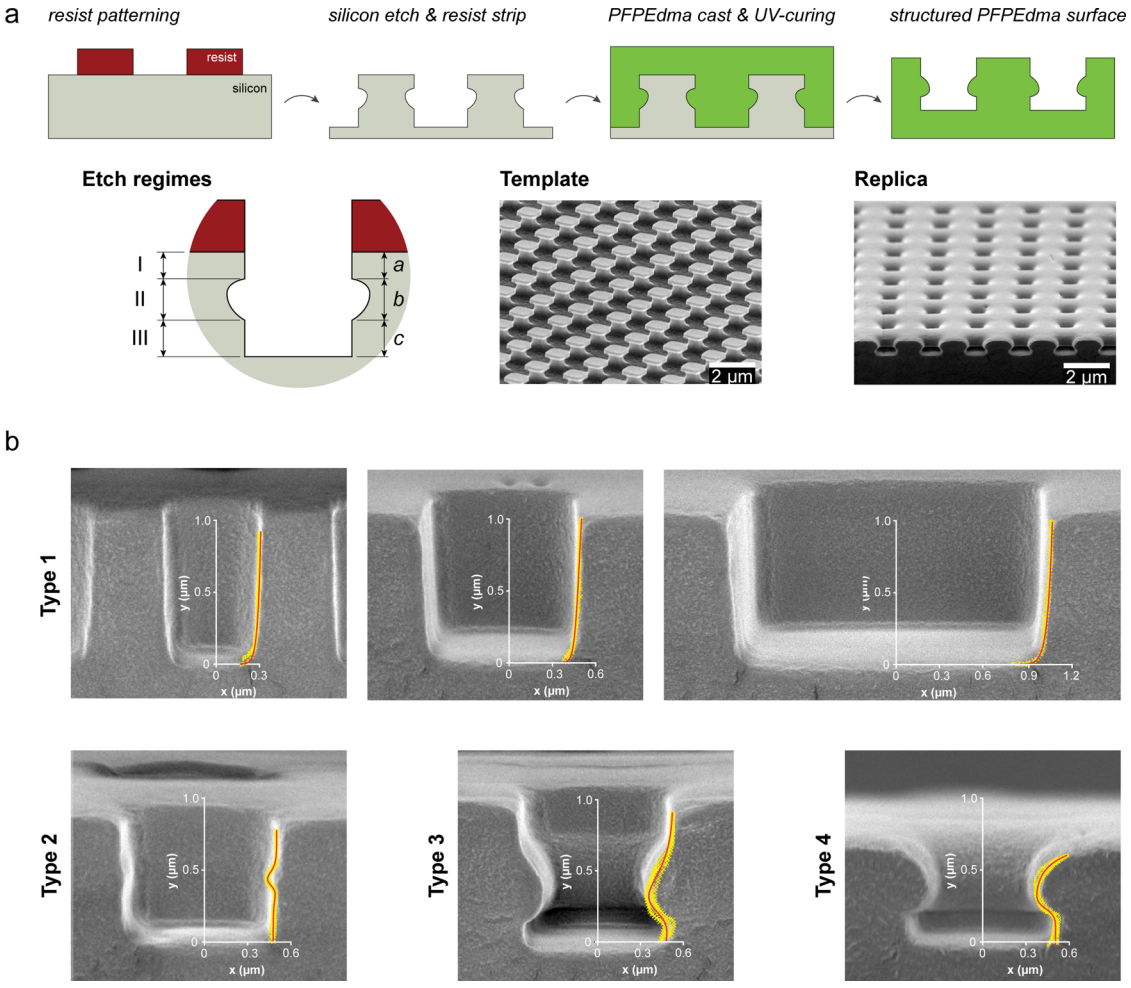

Figure 2. Textured perfluoropolyether dimethacrylate (PFPEdma) surfaces. (a) Process scheme for PFPEdma patterning: A silicon master structure is fabricated by optical lithography and subsequent pattern transfer by tunable silicon etches. The silicon master structure serves as template for replication into PFPEdma. (b) Variation of the cavity dimensions and cross-sectional sidewall profiles of the PFPEdma surfaces after cutting the samples. Yellow crosses show the estimated profile positions. Red lines represent the particular fit functions of each profile.

as their potential for self-recovery of the dewetted state was still lacking. Toward this aim, the present work experimentally explored the wetting transition for structured surfaces exhibiting different sidewall profiles. Various types of sidewall profiles were fabricated by an adaptive etching process applied to silicon masters, which were, in turn, replicated in perfluoropolyether dimethacrylate (PFPEdma), an intrinsically hydrophobic polymer material that exhibits a refractive index very close to the as refractive index of water. The wetting transition was recorded *in situ* upon hydrostatic pressure manipulation, and the recovery of partially dewetted cavities was analyzed upon pressure reduction and cyclic pressure variations. The obtained findings agreed well with the results of the developed model.

RESULTS AND DISCUSSION

Structured PFPEdma surfaces were cast from silicon masters serving as templates for the feature replication as schematically shown in Figure 2a. The silicon masters were fabricated by optical projection lithography using an i-line stepper and subsequent pattern transfer by reactive ion etching. By variation of the process parameters during etching, different sidewall profiles of the silicon patterns could be produced: Scallops and straight segments along the sidewalls were generated by isotropic (cf. regime II in Figure 2a) and anisotropic etch regimes (cf. regimes I and III in Figure 2a), respectively. For the surfaces of type 1, regime I was used to create pillars with straight sidewalls. In a top view, the pillars exhibit square shapes. The half-pitch of the patterns varied between 0.5, 1, and 2 μm, resulting in surface area fractions of about 0.75 for all fabricated surfaces. Several combinations of anisotropic and isotropic etching were used for the fabrication of surfaces of types 2−4. To explore the impact of the various different sidewall profiles, the half-pitch of the pillars was fixed to 1 μm for those types of structures. In Figure 2b, a sectional view of all fabricated surface patterns is displayed as a summary. The scanning electron micrographs represent the characteristic profiles and demonstrate the accurate transfer of overhangs or undercuts into the PFPEdma material.

Dynamic contact angle goniometry was carried out to evaluate the wetting characteristics of the differently structured PFPEdma surfaces for water droplets in reference to flat PFPEdma films (Figure 3). PFPEdma films are intrinsically hydrophobic, showing advancing contact angles of $\theta_{adv} \approx 108°$ and receding contact angles of $\theta_{rec} \approx 60°$. We found that the advancing and receding contact angles were slightly increased for all patterned surfaces, namely, $\theta_{adv} \approx 120°$ and $\theta_{rec} \approx 70°$, but without any characteristic variation between the different

dx.doi.org/10.1021/la503601u | *Langmuir* 2014, 30, 15162−15170

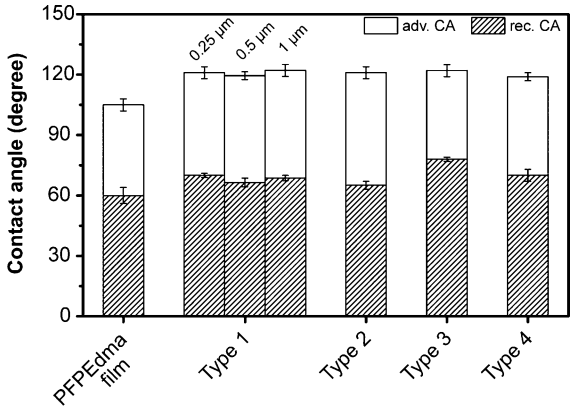

Figure 3. Advancing and receding water contact angles (CA) determined on the different types of textured PFPEdma surfaces in reference to flat PFPEdma films. For type 1 surfaces, the half-width of the cavities varied between 0.25, 0.5, and 1 μm, while for surfaces of types 2–4 the half-width of the cavities was fixed to 0.5 μm.

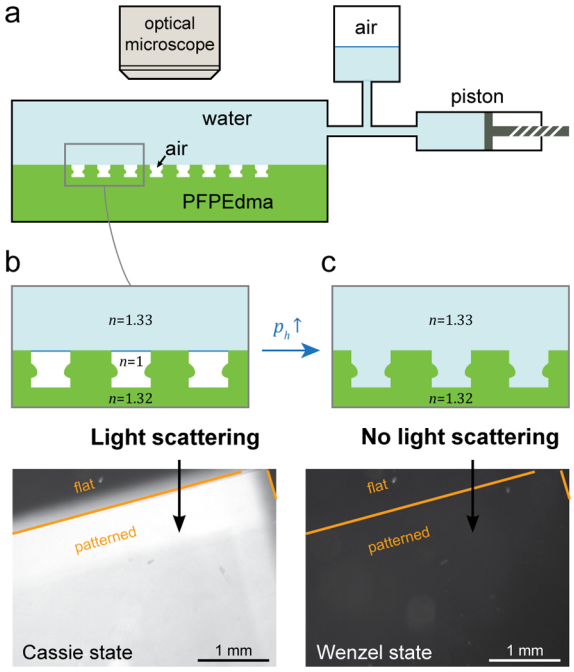

Figure 4. *In situ* observations of the Cassie–Wenzel transition. (a) Schematic illustration of the experimental setup that consists of an optical microscope, a piston, and a water-flooded chamber where the samples (green) are submerged. (b, c) The insets demonstrate the arrangement of the refractive indices, *n*, of water, air, and PFPEdma across the patterned interface: left and right insets refer to (b) the Cassie and (c) the Wenzel state, respectively. The micrograph shows the entrapped air (plastron) inside the cavities by a visible shiny appearance of scattered incoherent light in dark field illumination. (c) Disappearance of the shine was observed *in situ* while the hydrostatic pressure inside the aqueous phase is linearly increased.

types of textured surfaces. Because of the hydrophobic nature of the PFPEdma material, water wets only the top part of the patterns and air is kept entrapped inside the cavities underneath. Thus, the different sidewall profiles within the cavities do not influence the apparent contact angle. Interestingly, variation of the cavity dimensions (surface type 1) did not influence the apparent contact angles either. This finding is in accordance with the Cassie–Baxter model, according to which the apparent contact angle depends on the area fraction of the actually wetted area in relation to the projected solid surface area, but is independent from the actual pattern size.[34] Thus, for the investigated set of surface topographies contact angle goniometry did allow for dissecting differences neither in the surface feature size nor in the shape of the sidewall profiles.

Wetting transition tests upon complete immersion were performed to analyze the wetting barrier of the patterned PFPEdma surfaces. For that purpose, the samples were placed in a liquid-flooded chamber mounted on an optical microscope enabling *in situ* observations as schematically illustrated in Figure 4a.[12−14] Upon hydrostatic pressure manipulation, the changes in the scattered light intensity were monitored for an incoherent dark field illumination (see Supporting Information Movie M1). It was found that the intensity considerably varies between the Cassie and the Wenzel state, while the intensity on a flat reference surface did not change for different hydrostatic pressures (Figure 4b). This results from the fact that the refractive indices of water and PFPEdma are very similar (n_{water} = 1.33 and $n_{PFPEdma}$ = 1.32) and very different from the refractive index of air (n_{air} = 1.00). Consequently, in the Cassie state, light passing through the structured interface is scattered due to entrapped air pockets, resulting in a high intensity collected in the objective, while in the Wenzel state, the air pockets are replaced by water and the light passes an optically almost homogeneous interface with comparatively low scattering (Figure 4c). The obtained normalized intensities are displayed in Figure 5 for type 1 surfaces. The wetting transition was monitored as a characteristic drop of the intensity at a certain hydrostatic pressure. This value was found to significantly raise from about 300 hPa to values of about 1250 hPa for smaller cavities with half-width of x = 1 μm and x = 0.25 μm, respectively (Figure 5a). Thus, the Cassie–Wenzel transition barrier increases for smaller cavities (Figure 5b), according to the theoretical model summarized in eq 5.[20,35]

The transitions did not to occur at a specific pressure value, but covered, for example, a range in between 1250 and 1600 hPa for the smallest cavities (x = 0.25 μm). The observed range of transition pressure values originates from the experimental setup, which consists of the simultaneous observation thousands of cavities. Hence, the intensity curve represents statistical distributions due to deviations, e.g., in the cavities dimensions. Note that throughout this work, we defined the breakthrough pressure as the onset of the transition curve (cf. black arrows in Figure 5b).

Figure 6 displays the influence of the sidewall profiles on the wetting transition. The hydrostatic pressures required to induce the transition from the Cassie to the Wenzel state clearly differed for the compared surface types with 650 hPa for surface type 1, 800 hPa for surface type 2, and more than 2000 hPa for surface types 3 and 4. Except for type 1 surfaces, all cavity profiles had an inner constriction formed by scallops. Consequently, the distance between both sidewalls was decreased and the geometrical angle, Ψ, was increased, both resulting in elevated breakthrough pressures in accordance with eq 5. In addition, the intensity drops shown in Figure 6 are specific for the compared surface structure types and may be suitable to uncover the transition dynamics, in particular the enforced expansion of the fluid front into the cavities. For surface type 1, the wetting transition is characterized by a steeply sloping intensity above 650 hPa. Before the transition

dx.doi.org/10.1021/la503601u | *Langmuir* 2014, 30, 15162−15170

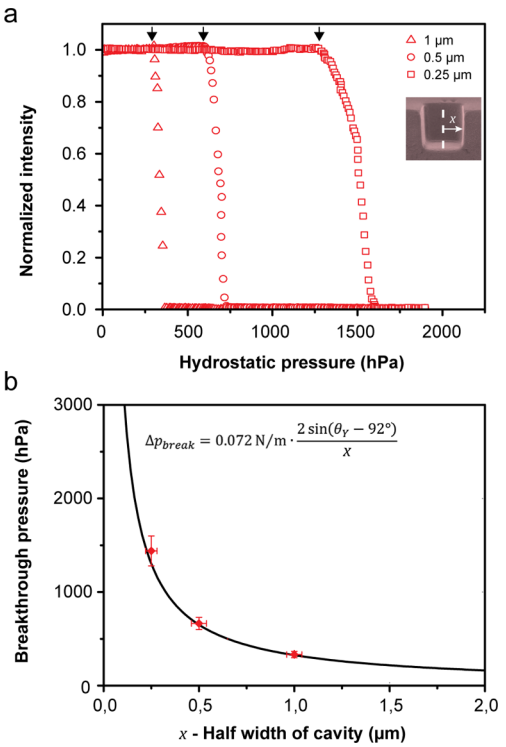

Figure 5. Influence of cavity dimensions on the wetting transition barrier of type 1 surfaces. (a) The drop of the normalized intensity of the scattered light from 1 to 0 represents the transition from the Cassie state to the Wenzel state. The black arrows represent the starting point of the transition that was used to define the breakthrough pressure. (b) Experimentally obtained (red diamonds) and calculated (eq 5, black line) breakthrough pressures (Δp_{break}) in relation to the half-width of the cavities, x.

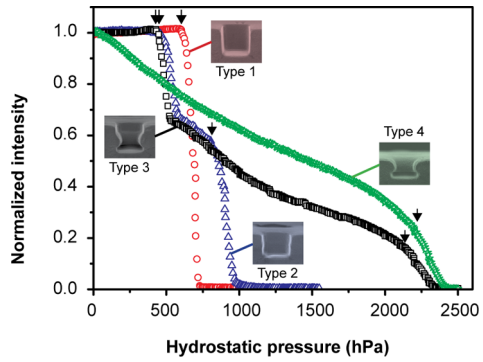

Figure 6. Impact of the shape of sidewall profiles on the wetting transition barrier. The decrease of the normalized intensity of the scattered light from 1 to 0 represents the transition from Cassie to Wenzel state. The shapes of the curves correlate to the penetration mechanisms of the expanding water front into the different types of cavities with a half-width of 0.5 μm (cf. Figure 2b).

occurs, the intensity remains almost constant (normalized value of 1). Thus, we suggest that the three-phase contact line sustained pinned before transition. For type 4 surfaces, in contrast, the intensity immediately decreases upon increasing the hydrostatic pressure. Before the actual breakthrough occurs, the normalized intensity already decreased to a value of about 0.3. Thus, we suggest that the three-phase contact line moves along the sidewall and the cavities are already partially filled before the transition occurs. For surface types 2 and 3, we observed a combination of the mechanisms occurring at type 1 and 4 surfaces, resulting in a stepwise transition: A first decrease in intensity occurs at a critical hydrostatic pressure as observed for type 1 surfaces. The transition is, however, interrupted at an intensity value of about 0.7. Subsequently, the intensity only slightly decreases until the final breakthrough occurs. Hence, the second transition step was similar to that found for type 4 surfaces.

The proposed mechanism of the two-step wetting transition seen for type 2 and 3 surfaces is illustrated in Figure 7. In the initial situation (Figure 7a), water is applied atop a cavity with the half-width, x_0. When the hydrostatic pressure is increased, the three-phase contact line is immediately pinned at the top edge of the cavity, i.e., the Cassie state, when $|\Psi_0| < \theta_Y$. As the hydrostatic pressure is equal to the atmospheric pressure of air entrapped inside the cavities, the initial liquid–air interface inside the cavity can be assumed to be planar ($\Delta p = 0$, cf. eq 4). The water–air interface sags into the cavity when the hydrostatic pressure is continuously increased due to the pinning of the three-phase contact line. The pinning is maintained until $\theta_{a,1} = \theta_Y + (\pi + \Psi_0)$, which is in line with the boundary condition of eq 3. A further increase of the hydrostatic pressure results in a downward sliding of the three-phase contact line along the cavity sidewall (Figure 7b), i.e., the first transition scenario. The transition is interrupted at the constriction of the cavity due to the scallop and the simultaneous change of the geometrical edge angle that results in a higher pressure barrier (Figure 7c) (cf. eq 5). Finally, after the second transition, the cavity is completely wetted; i.e., the Wenzel state is achieved (Figure 7d).

To investigate the recovery of the partially wetted state upon pressure reduction, the transition process was interrupted either rapidly, by opening the pressure control valve, or steadily, by a linear decrease of the hydrostatic pressure. In Figure 8a–c the recovery is displayed for surfaces of type 3, which exhibit a two-step transition process. Figure 8a gives a summary of the recovered intensities recorded upon pressure reduction for all applied preload pressures. Before the wetting transition occurs ($p_h < 500$ hPa), the three-phase contact line remains pinned at the top edge of the cavity, while the water–air interface sags into the cavity (slight increase in the intensity) with increasing hydrostatic pressure. Upon abrupt pressure reduction, the surface tension acts against the enforced curvature of the fluid interface, resulting in the complete recovery of the partially wetted state. After the first transition step ($500 < p_h < 2200$ hPa, cf. Figure 6), it was found that for all pressure preloads the recovered intensity was about 0.67. Once the second transition step occurred ($p_h > 2200$ hPa), completely wetted surfaces did not recover. The recovery of the partially wetted surface observed after the first transition step was further investigated by linear pressure cycles in the range of 0–2000 hPa. In Figure 8b the recorded hysteresis loop is shown. The intensity ranges between 0.25 and 0.65 for each cycle that relates to an enforced wetting and dewetting (recovery of partially wetted state) of the cavities. We assume that small differences between the intensity values at expansion and retraction of the fluid front relate to the differences between advancing and receding contact angles. The maximal recovery intensity was similar to the previously observed values obtained upon rapid pressure reduction. Thus, both experimental regimes demonstrated that the three-phase contact line is mobile at a certain section of the sidewall profile, which allows for partial reversibility of the enforced wetting of type 3 surfaces. Figure 8c gives a

dx.doi.org/10.1021/la503601u | Langmuir 2014, 30, 15162–15170

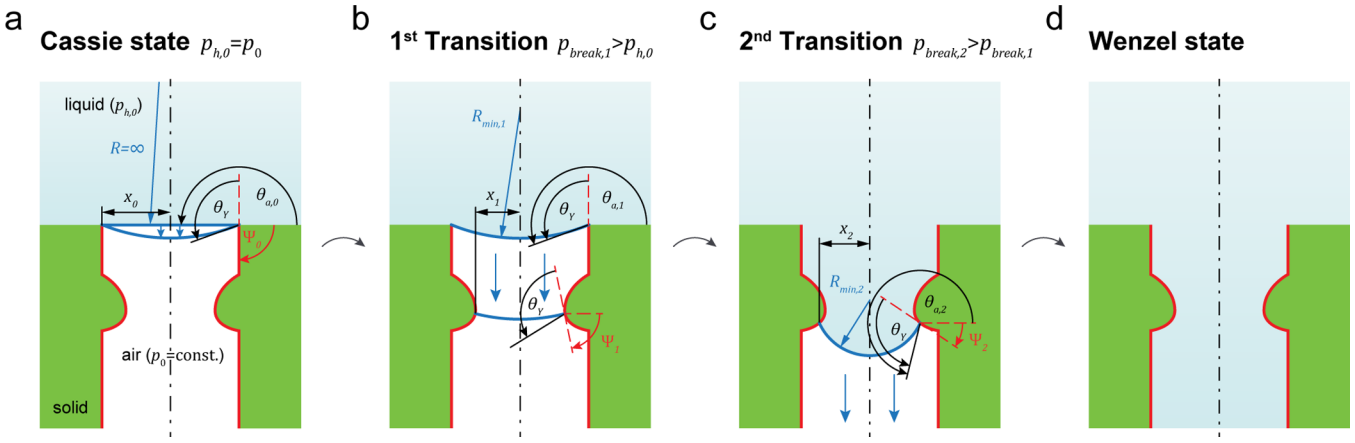

Figure 7. Schematic representation of the pressure-induced wetting transition. (a) Cassie state: liquid phase sustained atop a cavity with the half-width, x_0, the geometrical edge angle, Ψ_0, and the intrinsic contact angle, θ_Y. The initial hydrostatic pressure, p_h, is equal to the atmospheric pressure, p_0, inside the cavity. The liquid–air interface sags into the cavity (blue arrows) due to continuously increasing p_h while the three-phase contact line stays pinned. (b) The three-phase contact line slides downward the cavity sidewall (blue arrows) when the critical pressure $p_{break,1}$ is achieved and the apparent contact angle, $\theta_{a,1}$, of the sagging liquid–air interface becomes $\theta_Y + (\pi + \Psi_0)$ (eq 3). The transition is interrupted at the constriction of the cavity due to the scallop where x and Ψ changes. (c) The second transition takes place when the critical pressure $p_{break,2}$ is achieved and the apparent contact angle, $\theta_{a,2}$, of the sagging liquid–air interface becomes $\theta_Y + (\pi + \Psi_2)$. (d) Wenzel state: liquid phase completely wets the cavity.

comparison of the function of the sidewall profile (cf. Figure 2b) with the calculated Laplace pressure (eq 5) for each point along the profile. The function of the Laplace pressure has two local maxima at points 1 and 3 which both represent points of transition. At the first transition ($p_h > \Delta P_{break,1}$), the three-phase contact line slides along the profile and stops in between points 2 and 3. At this stage, the three-phase contact line can slide backward upon pressure reduction (p_h = 0 hPa) until it reaches point 2 where the Laplace pressure becomes zero. Between points 2 and 3, the three-phase contact line can move freely due to the steady increase in the Laplace pressure, which functions as restoring force once the pressure is reduced. At the second transition ($p_h > \Delta P_{break,2}$), the three-phase contact line is pushed over point 3, the restoring force drops, and consequently the liquid completely wets the cavity, corresponding to the Wenzel state.

Figure 8d–f displays the recovery effects on surfaces of type 4. Both the rapid and the steady decrease of hydrostatic pressure preloads feature an almost complete recovery (corresponding to intensity values of about 0.92; Figure 8d,e). The minor deviation from complete recovery can again be attributed to differences between the advancing and receding contact angles. Figure 8f gives a comparison of the function of the sidewall profile (cf. Figure 2b) with the calculated Laplace pressures (eq 4) for each point along the profile. The Laplace pressure function exhibits a zero point (point 1) and only one maximum localized at point 2, i.e., at the transition barrier. In between both points, the Laplace pressure steadily increases, and thus, the advancing and receding three-phase contact line can be moved along the sidewall by the hydrostatic pressure. After the transition point is reached ($p_h > \Delta P_{break}$), the liquid front completely wets the cavity, the interface attains the Wenzel state.

Taking together, the wetting transition correlates with the function of the Laplace pressure which depends on the sidewall profile of the surface features. Local maxima represent pressure barriers that need to be overcome for the wetting transition. In accordance with reports by Papadopoulos et al.,[26] the propagation of the fluid front can be extended over several minutes before reaching the maximum in the Laplace pressure function. In particular, the transition time corresponds to the velocity of the hydrostatic pressure elevation. After passing the maxima, the transition was observed to be abrupt as obvious from the drastic drop in scattered light intensity.

Of note, the striking differences in the results obtained for the compared structured surfaces suggest that air entrapped inside the cavities only plays a minor role in the recovery of the partially wetted state. Obviously, air compression can be neglected for the investigated system due to the high gas permeability of the PFPEdma material. These findings are in accordance with the so-called capillary burst microvalve effect that similarly describes the mechanism of propagating liquid fronts within diverging microfluidic channel sections.[36] Thus, the geometry determines the critical pressure differences before breakthrough. However, the effect of compressed air similarly depends on the time-dependent gas absorption of the liquid phase.

CONCLUSIONS

Using the similarity of the refractive index of hydrophobic PFPEdma to the one of water, we were able to investigate the pressure-induced wetting transition dynamics between the Cassie and the Wenzel state at a set of differently structured surfaces by recording scattered incoherent light. It was found that constrictions of surface textures, namely the shape of the sidewalls of grooves or cavities, can impact this wetting transition without influencing the apparent macroscopic contact angle. Consequently, the resistance against complete wetting can be manipulated independently, without affecting the repellence of the surfaces. Wetting recovery experiments revealed distinct positions at the sidewall profiles of the investigated surface structures, which correspond to irreversible or reversible wetting transitions. Thus, the shape of the sidewalls of surface features can support (or avoid) the recovery of the partially wetted state after temporary exposure of the surface to elevated hydrostatic pressures, for example, by impacting rain droplets.

dx.doi.org/10.1021/la503601u | Langmuir 2014, 30, 15162–15170

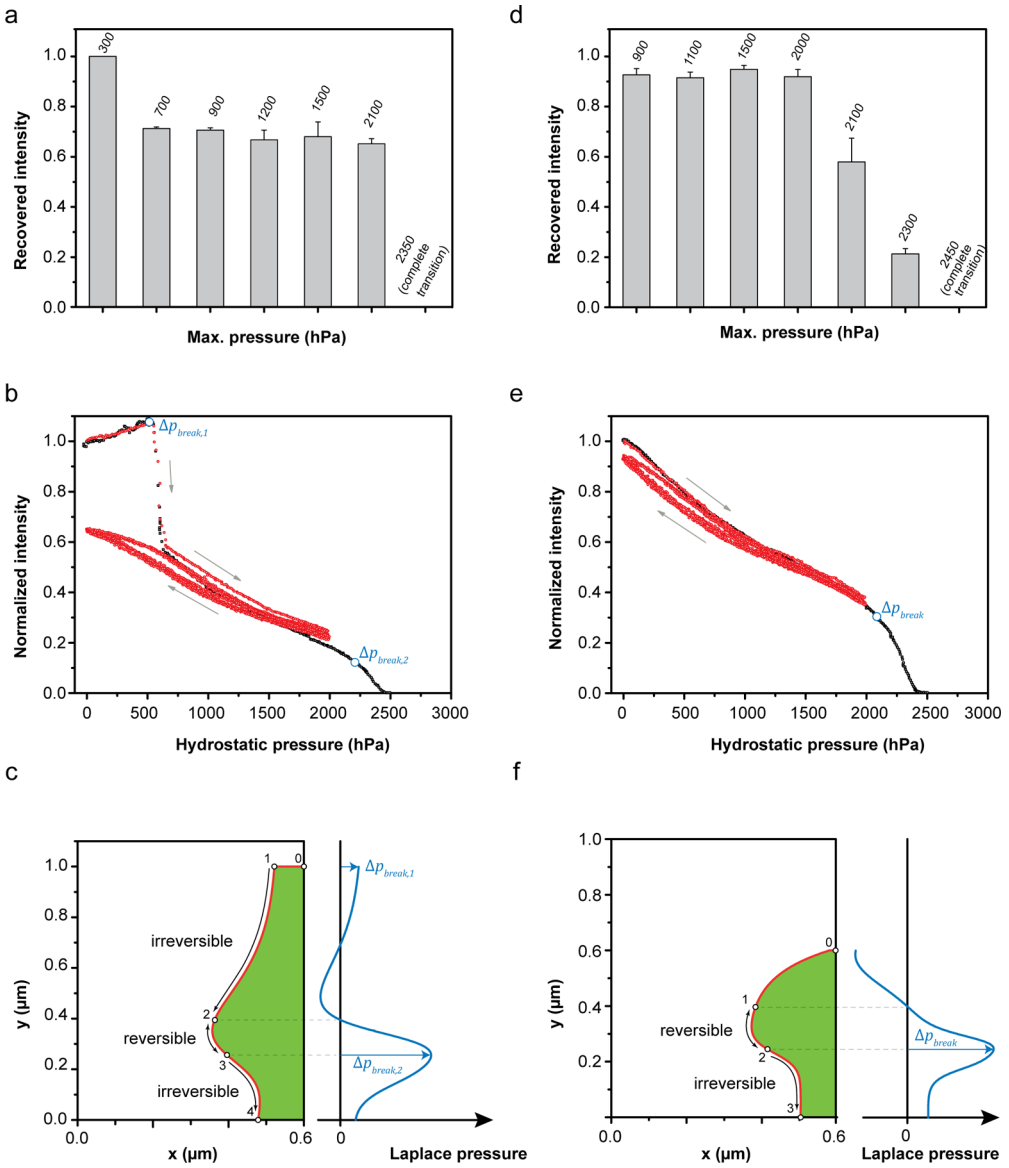

Figure 8. Wetting recovery effects on surfaces of type 3 (a–c) and type 4 (d–f). (a, d) Recovered intensity recorded upon abrupt reduction of the hydrostatic pressure by opening the pressure control valve in dependence on the previously loaded hydrostatic pressures. (b, e) Hysteresis of the normalized intensity by linear increase and decrease (10 hPa s^{-1}) of the hydrostatic pressure between 0 and 2000 hPa for 4 cycles (red dots) in reference to complete transition (black dots). (c, f) Characteristic fits (red curves) of the sidewall profile of (c) type 3 and (f) type 4 surfaces and their corresponding Laplace pressure (blue curves). The sections between points 0–4 represent characteristic parts along the profile including the initial wetted surface area, reversible, and irreversible transition regions.

MATERIALS AND METHODS

Sample Preparation. The sample preparation mainly consists of two steps: First, the fabrication of the silicon structures that, in turn, serve as templates for the polymer feature replication. Silicon structures were fabricated using a wafer-stepper exposure (PAS 5500-250C, ASML, Veldhoven, Netherlands) and subsequent pattern transfer using reactive ion etch processes (ASE System, STS, Newport, UK). The patterned area was 10 × 10 mm^2 for each structure type. To generate the different sidewall profiles, different etching regimes were combined, namely, a continuous (CE) and a pulsed etch process (PE). During the continuous etch process reactive gases for silicon etching (SF_6, 35 sccm, 10 mTorr) and sidewall passivation (C_4F_8, 85 sccm, 10 mTorr) are simultaneously inserted to the etching chamber to fabricate smooth sidewalls with sidewall angles of about 90°, i.e., an anisotropic etch regime.[37,38] For isotropic etching, one cycle of a pulsed etching process was utilized. In this regime, the sidewalls were passivated (C_4F_8, 85 sccm, 20 mTorr) first, and in a subsequent step the silicon was etched (SF_6, 130 sccm, 30 mTorr), resulting in a scallop, i.e., an isotropic etch regime. To generate the different sidewall profiles, both regimes were combined as following: type 1: (I) CE (270 s); type 2: (I) CE (120 s), (II) PE (passivation 8 s, etching 12 s), (III) CE (120 s); type 3: (I) CE (60 s), (II) PE (passivation 14 s, etching 21 s), (III) CE (90 s); type 4: (I) CE (60 s), (II) PE (passivation 14 s, etching 21 s), (III) CE (5 s).

After resist stripping, a perfluorododecyltrichlorosilane (Sigma-Aldrich, Deisenhofen, Germany) antisticking layer was applied to the silicon structures by molecular vapor deposition. The silicon structures were used as templates for casting the PFPEdma surfaces using Fomblin MD40 (Solvay Solexis, Bollate, Italy) precursor solution containing 0.5 wt % Irgacure 651 (CIBA, Basel, Switzerland).[39] The PFPEdma was cross-linked by UV-exposure (DELOLUX 04, DELO, Windach, Germany) for 5 min under a nitrogen atmosphere. The resulting structured PFPEdma surfaces were gently demolded and used for experiments without further (surface) modifications.

dx.doi.org/10.1021/la503601u | *Langmuir* 2014, 30, 15162–15170

The sidewall profiles of the different surface types were obtained from scanning electron micrographs by measuring points of the cross section after cutting the samples using the open-source software ImageJ, v. 1.43.[40] Data of at least four different measurements were subsequently fitted by the following functions: type 1: $f_n(x) = A \exp^{x/t} + B$; types 2−4: $f_n(x) = A + (B - A)/(1 + 10^{(x-x_1)t_1}) + (C - A)/(1 + 10^{(x_2 - x)t_2})$ and utilized for further calculations, namely, the determination of the geometrical angle, $\Psi = \tan^{-1} f_n'(x)$ (applied with Origin, OriginLab, v. 8.6). The origin of each coordinate system was set to be at the bottom center of each cavity.

Ellipsometry. To determine the refractive index of the cross-linked PFPEdma polymer, ellipsometry was utilized. Therefore, thin PFPEdma films were prepared by spin-coating of 1 part of MD40 diluted in 100 parts of FC-75 (3M, Haven, Belgium) on silicon wafer with 30 nm silicon dioxide on top. The refractive index of PFPEdma was determined by using a multiwavelength ellipsometer (alpha-SE, J.A. Wollam Co., Lincoln, NE) in the spectral range of 380−900 nm and incidence angles of 60°, 65°, and 70°. The refractive index was calculated from obtained ellipsomatric data using the model (Si/SiO_2/polymer/ambient) and the Cauchy relation to describe the wavelength dependence of the refractive index of the polymer.[41]

Contact Angle Goniometry. To determine the wetting characteristics of the structured PFPEdma surfaces in reference to smooth polymer films, dynamic contact angle measurements were performed using a contact angle measurement system OCA 30 (DataPhysics Instruments, Filderstadt, Germany). Droplets (10 μL) of Milli-Q filtered water (Merck Millipore, Billerica, MA) were applied to the surfaces. The droplet was inflated and deflated (0.5 μL/s) to monitor the advancing and the receding contact angle, respectively.

Wetting Transition Tests. Wetting transition experiments were performed using a customized setup previously reported.[12−14] Briefly, the setup consisted of an optical microscope, a piston, a processing unit and a chamber flooded by water (cf. Figure 4). Once the samples were immersed completely, the Cassie−Wenzel transitions were induced by linearly compressing (10 hPa s^{-1}) the liquid reservoir to increase the hydrostatic pressure. *In situ* monitoring the intensity of the scattered light in dark field configuration was performed using an optical microscope (Axiotech, Zeiss, Jena, Germany). The intensity of the scattered light was recorded using a CCD sensor. The obtained changes in the gray value were analyzed and normalized using the open-source software ImageJ, v. 1.43.[40] To minimize the influence of the gas solubility in water, the experiments were carried out at a water−air ratio of about 10:1. Recovery tests were performed by interrupting the compression either by quick reduction due to opening of the pressure control valve or by a controlled linear decrease (10 hPa s^{-1}) of the hydrostatic pressure.

SEM Imaging. SEM images were recorded using a DSM 982 (Carl Zeiss SMT, Oberkochen, Germany). All samples were coated with approximately 3 nm platinum (BAL-TEC SCD 500, BalTec, Pfäffikon, Switzerland) to eliminate surface charging effects.

■ ASSOCIATED CONTENT

Supporting Information

Movie M1 demonstrating the changes in the scattered light intensity while the wetting transition occurs. This material is available free of charge via the Internet at http://pubs.acs.org.

■ AUTHOR INFORMATION

Corresponding Authors

*E-mail rene.hensel@inm-gmbh.de; phone +49 681 9300 390 (R.H.).

*E-mail werner@ipfdd.de; phone +49 351 4658 531; Fax +49 351 4658 533 (C.W.).

Present Address

R.H.: INM−Leibniz Institute for New Materials, 66123 Saarbrücken, Germany.

Notes

The authors declare no competing financial interest.

■ ACKNOWLEDGMENTS

We are grateful to Dr. Ralf Zimmermann and Susanne Bartsch (Max Bergmann Center of Biomaterials, Leibniz Institute of Polymer Research, Dresden, Germany) for determination of the refractive index of PFPEdma (MD40, Solvay Solexis). Re.H. and A.F. were funded by the DFG Research Training Group 1401/2 "Nano- and Biotechnologies for Packaging of Electronic Systems". In addition, Re.H. was funded by the ERC Grant 340929 at the INM. Ra.H. was funded by DFG WE 2539/17-1 and S.K. by the ESF Junior Research Group "3CSI-3D Chip Stack Intraconnects".

■ REFERENCES

(1) Wenzel, R. Resistance of solid surfaces to wetting by water. *Ind. Eng. Chem.* **1936**, *28*, 988−994.

(2) Cassie, A.; Baxter, S. Wettability of porous surfaces. *Trans. Faraday Soc.* **1944**, *40*, 546−551.

(3) Marmur, A. Wetting on hydrophobic rough surfaces: to be heterogeneous or not to be? *Langmuir* **2003**, *19*, 8343−8348.

(4) Marmur, A. From hygrophilic to superhygrophobic: Theoretical conditions for making high-contact-angle surfaces from low-contact-angle materials. *Langmuir* **2008**, *24*, 7573−7579.

(5) Ishino, C.; Okumura, K.; Quéré, D. Wetting transitions on rough surfaces. *Europhys. Lett.* **2004**, *68*, 419.

(6) Quéré, D. Wetting and roughness. *Annu. Rev. Mater. Res.* **2008**, *38*, 71−99.

(7) Marmur, A. Solid-surface characterization by wetting. *Annu. Rev. Mater. Res.* **2009**, *39*, 473−489.

(8) Bormashenko, E. Progress in understanding wetting transitions on rough surfaces. *Adv. Colloid Interface Sci.* **2014**, DOI: 10.1016/j.cis.2014.02.009.

(9) Xue, Y.; Chu, S.; Lv, P.; Duan, H. Importance of hierarchical structures in wetting stability on submersed superhydrophobic surfaces. *Langmuir* **2012**, *28*, 9440−9450.

(10) Soto, D.; De Larivière, A. B.; Boutillon, X.; Clanet, C.; Quéré, D. The force of impacting rain. *Soft Matter* **2014**, *10*, 4929−4934.

(11) Moulinet, S.; Bartolo, D. Life and death of a fakir droplet: impalement transitions on superhydrophobic surfaces. *Eur. Phys. J. E* **2007**, *24*, 251−260.

(12) Helbig, R.; Nickerl, J.; Neinhuis, C.; Werner, C. Smart skin patterns protect springtails. *PLoS One* **2011**, *6*, e25105.

(13) Hensel, R.; Helbig, R.; Aland, S.; Voigt, A.; Neinhuis, C.; Werner, C. Tunable nano-replication to explore the omniphobic characteristics of springtail skin. *NPG Asia Mater.* **2013**, *5*, e37.

(14) Hensel, R.; Finn, A.; Helbig, R.; Braun, H.-G.; Neinhuis, C.; Fischer, W.-J.; Werner, C. Biologically inspired omniphobic surfaces by reverse imprint lithography. *Adv. Mater.* **2014**, *26*, 2029−2033.

(15) Bormashenko, E.; Pogreb, R.; Whyman, G.; Erlich, M. Cassie-Wenzel wetting transition in vibrating drops deposited on rough surfaces: Is the dynamic Cassie-Wenzel wetting transition a 2D or 1D affair? *Langmuir* **2007**, *23*, 6501−6503.

(16) Krupenkin, T. N.; Taylor, J. A.; Wang, E. N.; Kolodner, P.; Hodes, M.; Salamon, T. R. Reversible wetting−dewetting transitions on electrically tunable superhydrophobic nanostructured surfaces. *Langmuir* **2007**, *23*, 9128−9133.

(17) Whyman, G.; Bormashenko, E. How to make the Cassie wetting state stable? *Langmuir* **2011**, *27*, 8171−8176.

(18) Barbieri, L.; Wagner, E.; Hoffmann, P. Water wetting transition parameters of perfluorinated substrates with periodically distributed flat-top microscale obstacles. *Langmuir* **2007**, *23*, 1723−1734.

(19) Butt, H.-J.; Roisman, I. V.; Brinkmann, M.; Papadopoulos, P.; Vollmer, D.; Semprebon, C. Characterization of super liquid-repellent surfaces. *Curr. Opin. Colloid Interface Sci.* **2014**, DOI: 10.1016/j.cocis.2014.04.009.

(20) Hensel, R.; Helbig, R.; Aland, S.; Braun, H.-G.; Voigt, A.; Neinhuis, C.; Werner, C. Wetting resistance at its topographical limit - The benefit of mushroom and serif T structures. *Langmuir* **2013**, *29*, 1100−1112.
(21) Oliver, J. F.; Huh, C.; Mason, S. G. Resistance to spreading of liquids by sharp edges. *J. Colloid Interface Sci.* **1977**, *59*, 568−581.
(22) Berthier, J.; Loe-Mie, F.; Tran, V.; Schoumacker, S.; Mittler, F.; Marchand, G.; Sarrut, N. On the pinning of interfaces on micropillar edges. *J. Colloid Interface Sci.* **2009**, *338*, 296−303.
(23) Extrand, C.; Moon, S. Influence of geometry, edges and roughness on liquid penetration and removal during wet cleaning. *ECS J. Solid State Sci. Technol.* **2014**, *3*, P198−P200.
(24) Hampton, M. J.; Williams, S. S.; Zhou, Z.; Nunes, J.; Ko, D.-H.; Templeton, J. L.; Samulski, E. T.; DeSimone, J. M. The patterning of sub-500 nm inorganic oxide structures. *Adv. Mater.* **2008**, *20*, 2667−2673.
(25) Semprebon, C.; Forsberg, P. S. H.; Priest, C.; Brinkmann, M. Pinning and wicking in regular pillar arrays. *Soft Matter* **2014**, *10*, 3254−3258.
(26) Papadopoulos, P.; Mammen, L.; Deng, X.; Vollmer, D.; Butt, H.-J. How superhydrophobicity breaks down. *Proc. Natl. Acad. Sci. U. S. A.* **2013**, *110*, 3254−3258.
(27) Antonini, C.; Lee, J.; Maitra, T.; Irvine, S.; Derome, D.; Tiwari, M. K.; Carmeliet, J.; Poulikakos, D. Unraveling wetting transition through surface textures with X-rays: Liquid meniscus penetration phenomena. *Sci. Rep.* **2014**, *4*, 4055.
(28) Haimov, B.; Pechook, S.; Ternyak, O.; Pokroy, B. Shape of water-air interface beneath a drop on a superhydrophobic surface revealed: Constant curvature that approaches zero. *J. Phys. Chem. C* **2013**, *117*, 6658−6663.
(29) Lv, P.; Xue, Y.; Shi, Y.; Lin, H.; Duan, H. Metastable states and wetting transition of submerged superhydrophobic structures. *Phys. Rev. Lett.* **2014**, *112*, 196101.
(30) Li, S.; Lamant, S.; Carlier, J.; Toubal, M.; Campistron, P.; Xu, X.; Vereecke, G.; Senez, V.; Thomy, V.; Nongaillard, B. High-frequency acoustic for nanostructure wetting characterization. *Langmuir* **2014**, *30*, 7601−7608.
(31) Bobji, M. S.; Kumar, S. V.; Asthana, A.; Govardhan, R. N. Underwater sustainability of the "Cassie" state of wetting. *Langmuir* **2009**, *25*, 12120−12126.
(32) Lei, L.; Li, H.; Shi, J.; Chen, Y. Diffraction patterns of a water-submerged superhydrophobic grating under pressure. *Langmuir* **2009**, *26*, 3666−3669.
(33) Samaha, M. A.; Ochanda, F. O.; Tafreshi, H. V.; Tepper, G. C.; Gad-el Hak, M. In situ, noninvasive characterization of superhydrophobic coatings. *Rev. Sci. Instrum.* **2011**, *82*, 045109.
(34) Note that this is true for drop sizes larger than a few nanometers and smaller than the capillary length of the applied liquid.
(35) Note that for all calculations throughout this work the square-shaped cross section of the cavities was assumed to be circular with setting the side length of the square equal to the radius of the cavity.
(36) Cho, H.; Kim, H.-Y.; Kang, J. Y.; Kim, T. S. How the capillary burst microvalve works. *J. Colloid Interface Sci.* **2007**, *306*, 379−385.
(37) He, J.; Richter, K.; Bartha, J.; Howitz, S. Fabrication of silicon template with smooth tapered sidewall for nanoimprint lithography. *J. Vac. Sci. Technol., B* **2011**, *29*, 06FC16.
(38) Finn, A.; Hensel, R.; Hagemann, F.; Kirchner, R.; Jahn, A.; Fischer, W.-J. Geometrical properties of multilayer nano-imprint-lithography molds for optical applications. *Microelectron. Eng.* **2012**, *98*, 284−287.
(39) Hensel, R.; Braun, H.-G. Free-floating hydrogel-based rafts supporting a microarray of functional entities at fluid interfaces. *Soft Matter* **2012**, *8*, 5293−5300.
(40) Rasband, W. ImageJ, 1997−2012; http://imagej.nih.gov/ij/.
(41) Richter, A.; Janke, A.; Zschoche, S.; Zimmermann, R.; Simon, F.; Eichhorn, K.-J.; Voit, B.; Appelhans, D. pH-stable hyperbranched poly (ethyleneimine)-maltose films for the interaction with phosphate containing drugs. *New J. Chem.* **2010**, *34*, 2105−2108.